

ARTICLE OPEN



Two-dimensional ferromagnetism detected by proximity-coupled quantum Hall effect of graphene

Tuan Khanh Chau^{1,4}, Sung Ju Hong^{2,4}, Haeyong Kang³ and Dongseok Suh¹✉

The recent discovery of a two-dimensional van der Waals magnet has paved the way for an enhanced understanding of two-dimensional magnetic systems. The development of appropriate heterostructures in this emerging class of materials is required as the next step towards applications. Here, we report on the electrical transport in monolayer graphene coupled with the two-dimensional ferromagnet Cr₂Ge₂Te₆ (CGT). Graphene that forms an interface with CGT is electron-doped owing to charge transfer. The temperature-dependent resistance of graphene/CGT undergoes a nontrivial sudden change near the Curie temperature (T_c) of CGT. Apart from this, the behavior of various transport parameters also differs before and after T_c . Moreover, the contribution of the magnetization of CGT to the enhanced magnetic flux density leads to the critical evolution of the quantum Hall state. These results imply that graphene in the graphene/CGT hybrid structure can be utilized to electrically monitor the magnetic phase transition of the adjacent CGT layer.

npj Quantum Materials (2022)7:27; <https://doi.org/10.1038/s41535-022-00435-9>

INTRODUCTION

The electrical properties of graphene are extremely sensitive to its environmental surroundings. Thus, suspended structures or particular substrates, such as hexagonal boron nitride (h-BN), have been employed to promote device performance with high mobility^{1–3}. In addition to device improvement, the formation of superlattices by utilizing substrates with a similar atomic registry has paved the way to explore emergent studies in condensed matter physics (e.g., Moiré superlattices, unconventional superconductivity, and Mott insulators)^{4–11}. Furthermore, intensive efforts have been devoted to realizing various functionalities by employing the proximity effect with ferroelectric, ferromagnetic, and multiferroic materials^{12–23}. As a result, fascinating device concepts have been suggested by applying the proximity effect to graphene.

In particular, studies on the magnetic proximity effect were carried out only for thin films because two-dimensional (2D) magnetism was expected to be absent due to thermal fluctuation, according to the Mermin–Wagner theorem²⁴. However, various 2D magnetic materials (Cr₂Ge₂Te₆, CrI₃, Fe₃GeTe₂, etc.) were recently reported such that abundant proximity-induced phenomena, both fundamental and practical, are anticipated^{25–30}. Among these magnetic materials, Cr₂Ge₂Te₆ (CGT) offers advantages that include facile exfoliation, stability in the air, and an insulating nature, which enable the investigation of the electrical properties of a van der Waals (vdW) heterostructure such as those of the graphene/2D magnetic material. Monitoring the electrical properties of a graphene/2D magnet is of significance for two reasons. The first is the induction of spin-related transport in graphene for spintronic applications^{13,15,19,31–35}. The second, which is less well known, is that it allows the phase transition of a 2D magnet to be monitored²¹. Given that only magnetic properties such as magnetization can be studied in magnetic insulators, the fact that graphene can detect changes in adjacent 2D magnets provides a versatile route for investigating the phase transition.

Here, we report on the modification of the properties of graphene resulting from the magnetic-proximity effect of CGT. Prior to studying graphene/CGT, we characterized the electrical properties of pristine CGT using a graphene electrode to show that the results are consistent with those of previous studies. Then we examined the graphene/CGT to determine the influence of CGT on graphene, which exhibits many proximity-induced phenomena, including electron doping owing to charge transfer and the nontrivial temperature dependence of the transport properties related to the phase transition in CGT. The ability to detect changes in its environmental surroundings renders the graphene field-effect transistor a platform for studying various phases in magnetic insulators.

RESULTS

Device fabrication and characterization of pristine CGT and graphene/CGT

The left panel of Fig. 1a exhibits a conceptual schematic of graphene/CGT heterostructure on h-BN, where the magnetization of CGT couples with graphene. The right panel of Fig. 1a shows a schematic representation (upper panels) and optical images (lower panels) of the graphene/CGT device (Device #1, D1). The device structure comprises exfoliated monolayer graphene placed on the bottom h-BN flake, which is followed by the transfer of the CGT and the top h-BN layers. Two types of graphene, patterned in the shapes of (i) two electrodes and (ii) a Hall-bar structure shown in Fig. 1a, were adopted to investigate the electrical properties of pristine CGT and graphene/CGT, respectively. It should be noted that the graphene and the CGT flakes were weakly coupled in our experiment, which may have resulted from the short-term exposure to air during the transfer of exfoliated CGT flakes (see Supplementary Fig. 1). Despite the weak coupling, as we show in the following results, the magnetic phase transition in CGT was

¹Department of Energy Science, Sungkyunkwan University, Suwon, Republic of Korea. ²Division of Science Education, Kangwon National University, Chuncheon, Republic of Korea. ³Department of Physics, Pusan National University, Busan, Republic of Korea. ⁴These authors contributed equally: Tuan Khanh Chau, Sung Ju Hong. ✉email: energy.suh@skku.edu

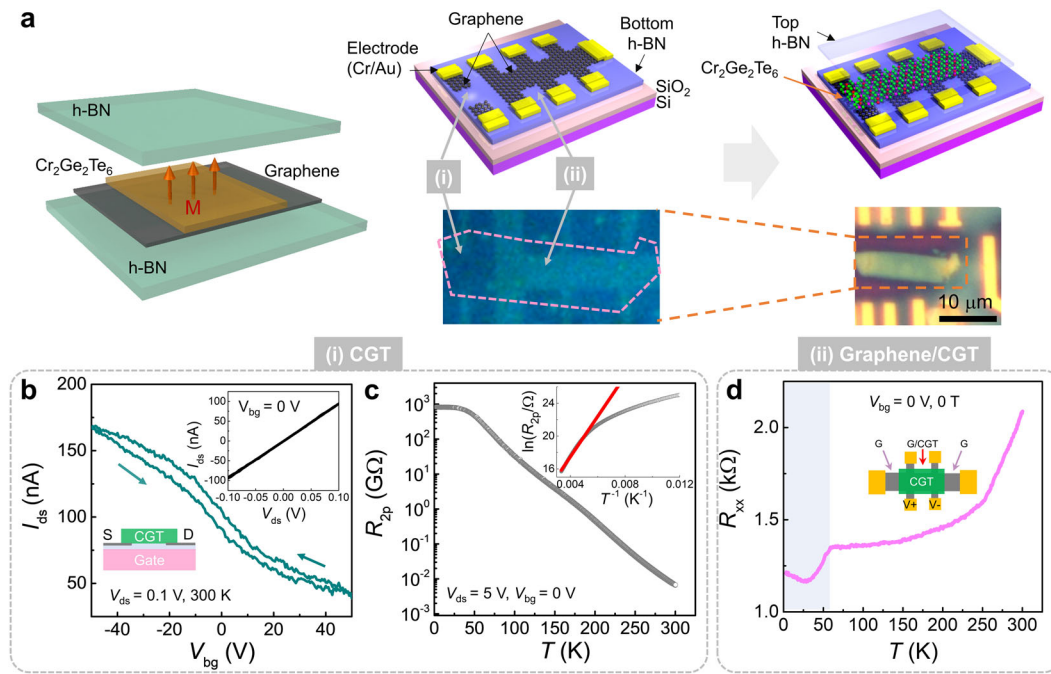


Fig. 1 Fabrication of graphene/CGT heterostructures and temperature-dependent resistance of pristine CGT and graphene/CGT. **a** Conceptual drawing of the heterostructure (left), optical and schematic images of patterned graphene (center) and graphene/CGT (right) for sample D1; (i) and (ii): patterned graphene used to study the electrical properties of pristine CGT and graphene/CGT, respectively. **b** Transfer characteristic curve (I_{ds} vs. V_{bg}) of CGT exhibiting p -type behavior. The lower left inset is a side-view schematic of the CGT transistor with a graphene electrode. The upper right inset shows the I_{ds} - V_{ds} curve of CGT measured using the graphene electrode in 2P configuration. **c** Temperature-dependent resistance of CGT at $V_{ds} = 5$ V and $V_{bg} = 0$ V. The inset shows the Arrhenius plot of the results, where the red fitted line yields an energy gap of ~ 0.42 eV. **d** Temperature-dependent R_{xx} of graphene/CGT at $V_{bg} = 0$ V and 0 T. The inset shows a top-view schematic of the measurement configuration.

sensitively monitored through the electrical transport in graphene, including the quantum Hall phenomena.

We characterized the electrical properties of pristine CGT (located across two graphene electrodes, marked as region (i)) in Fig. 1b, c. The inset in Fig. 1b shows that the graphene-CGT-graphene series resistance is ohmic in the two-probe (2P) configuration. The transfer characteristic curve of CGT in Fig. 1b exhibits p -type semiconductor behavior at room temperature^{36–38}. Figure 1c indicates the temperature-dependent resistance with back-gate voltage (V_{bg}) of 0 V, showing nonmetallic behavior in the low-temperature regime. The magnitude of R_{2p} is of the order of $10^6 \Omega$ near room temperature and increases to $10^{12} \Omega$ at the lowest temperature of 2 K. The thermal activation energy gap, estimated from the relation $R_{2p} \propto \exp(E_g/2k_B T)$, where k_B is Boltzmann's constant, is $E_g \sim 0.42$ eV according to the linear fitting of the Arrhenius plot in the inset in Fig. 1c. The order of magnitude of this gap is the same as the previously reported values of ~ 0.2 eV³⁹ and ~ 0.8 eV⁴⁰. From the viewpoint of graphene/CGT to be discussed below, the charge transport of CGT can be ignored owing to its extremely high resistance compared with that of graphene.

A more significant result is observed for the temperature-dependent resistance (R_{xx} vs. T) of the graphene/CGT device (region (ii)), where CGT is located on top of the graphene Hall bar, in Fig. 1d. The temperature dependence of R_{xx} shows kink-like behavior near the temperature of 60 K, which corresponds to the Curie temperature ($T_c \sim 61$ K) of CGT for the ferromagnetic transition²⁵. In general, phonon scattering (in the metallic regime, $dR_{xx}/dT > 0$) and thermal activation (in the insulating regime, $dR_{xx}/dT < 0$) were extensively discussed in a review on the transport of pristine graphene⁴¹. However, their common feature is that R_{xx} vs. T changes smoothly rather than abruptly. Therefore, the peculiar change near 60 K in Fig. 1d for the graphene/CGT device can be

attributed to extrinsic effects: the magnetic-phase transition of CGT in this case.

Charge transfer between graphene and CGT

We also observed n -type doping in the graphene underneath the CGT above T_c as shown in Fig. 2. Schematic illustrations of two different device configurations (type A and B) are presented in Fig. 2a, c, respectively. For type A, which corresponds to samples D1 and D2, graphene was patterned in the shape of a Hall bar and partially covered by the CGT flake in the region of its internal voltage probes. The resistance of the sample was measured in two different ways. The first is the 2P configuration using the probes at both ends of the sample (as marked with red lines in Fig. 2a), where the measured resistance (R_{2p}) is the addition of the resistance of both pristine graphene, and that of graphene/CGT connected in series. The other involved the use of the four-probe (4P) configuration to measure the resistance value (R_{xx}) of graphene/CGT only, because the voltage probes are entirely covered by the CGT flake.

Figure 2b shows the transfer-characteristic curves of sample D1 at 80 K. The 2P measurement indicates that R_{2p} exhibits two distinct peaks at $V_{bg} = -11$ V and 3 V, indicating that two types of graphene channel with different carrier density are connected in series⁴². However, R_{xx} in the 4P measurement exhibits a single peak at $V_{bg} = -11$ V, yielding the electrical property of only graphene/CGT. The well-matched peaks at $V_{bg} = -11$ V in both data curves surely correspond to the Dirac point (V_{DP}) of graphene/CGT. The observation that V_{DP} of graphene/CGT is more negative than that of pristine graphene reveals that electron doping occurred as a result of charge transfer between graphene and CGT. This electron doping effect is repeatedly observed in a different device configuration, type B shown in Fig. 2c, where many R_{2p} electrode pairs are formed in the same sample, and one of them is covered by CGT. The sample D3

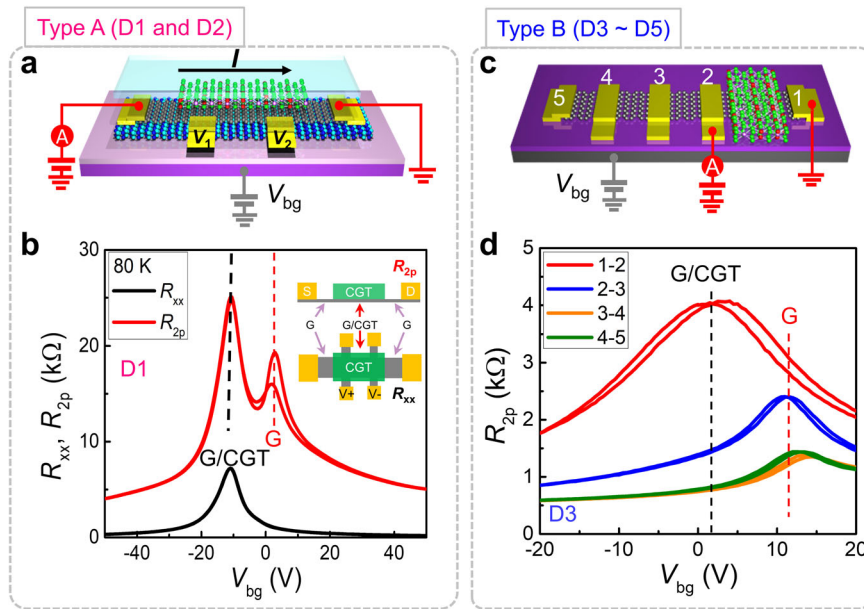


Fig. 2 Electron doping of graphene due to charge transfer from CGT. **a, c** Schematic illustration of device type A (D1 and D2) and B (D3–D5), respectively. For type A, 2P (red) and 4P (black) configurations are adopted. For type B, only the 2P configuration is used. **b, d** Corresponding transfer-characteristic curves of D1 and D3. Inset of **(b)** shows schematic diagrams for the measurement configuration of R_{2p} (upper) and R_{xx} (lower), where the upper and lower illustrations are the side and top views, respectively.

gives $V_{DP} = 2\text{V}$ for graphene/CGT and $V_{DP} = 12\text{V}$ for pristine graphene as in Fig. 2d. In addition to samples D1 and D3, other samples, D2 (type A) and D4 (type B), also exhibit reproducible electron doping effects as summarized in Supplementary Table 1. Moreover, all of these devices exhibit a similar electron doping level of $\sim 7.58 \times 10^{11}\text{ cm}^{-2}$ as an average density. This feature may be related to the charge transfer originating from the difference in the work function between graphene and CGT⁴³.

Critical behavior due to proximity coupling

By focusing on the ferromagnetic phase of CGT below $T_c \sim 61\text{ K}$, we observe a clear change in the transport parameters of graphene/CGT, which are collectively shown in Fig. 3. The V_{bg} -dependent longitudinal resistance curves of sample D1 at 80 K and 2 K are presented in Fig. 3a. At 80 K, R_{xx} undergoes no hysteresis when the V_{bg} sweep direction is reversed, whereas hysteresis is observed at 2 K. The ΔV_{DP} data, defined as the difference between V_{DP} values in the opposite V_{bg} sweep directions, are plotted as a function of temperature in the upper panel of Fig. 3e. Hysteresis (represented by $\Delta V_{DP} \neq 0$) exists in the temperature region below 60 K, but disappears (with $\Delta V_{DP} = 0$) at temperatures above 60 K. The inset shows the raw data of V_{DP} that were used for estimating ΔV_{DP} . Hysteresis in the R_{xx} vs. V_{bg} transfer curves is usually ascribed to the effect of charge traps near the channel, where the trapping and releasing processes are controlled by the gate bias⁴⁴. Even though the energy trap can be deepened as the temperature decreases, the sudden emergence of hysteresis near 60 K cannot be easily understood without a correlation with the ferromagnetic phase transition of CGT. Furthermore, similar hysteresis is observed in the quantum Hall (QH) state at the temperature of 2 K and magnetic field of 14 T as in Fig. 3b. The fact that charge traps usually induce strong Coulomb scattering and hinder the appearance of clear QH states seems to suggest that the charge traps are spatially apart from the graphene channel in this graphene/CGT device.

We also confirmed the coupling between graphene and CGT located in close proximity by investigating the magneto-transport properties of the graphene/CGT device. Figure 3c, d show graphs of R_{xx} and R_{xy} vs. $\mu_0 H$ of sample D1 at various temperatures

between 2 K and 150 K, respectively, where μ_0 is the vacuum permeability and H is the magnetic field strength. The QH states of monolayer graphene, corresponding to the quantized Hall resistance of $h/2e^2$ and $h/6e^2$, in which h is Planck's constant and e is the charge element, exist in the low-temperature regime. However, unlike the general QH feature of pristine graphene where the positions of QH plateaus or R_{xx} peaks are fixed for a given V_{bg} ^{45,46}, the position of the R_{xx} peak of the graphene/CGT device in Fig. 3c shifts towards the high-magnetic field regime as the temperature decreases from 60 K (orange dot) to 2 K (black dot). This tendency is confirmed in the second panel of Fig. 3e, which shows the temperature dependency of the R_{xx} peak. Interestingly, the R_{xx} peak does not shift markedly at temperatures above 60 K.

The Hall carrier density (n_{Hall}) is obtained from the slope of the R_{xy} data curves, i.e., $dR_{xy}/d(\mu_0 H)$, at low magnetic fields (between -1 T and 1 T) in Fig. 3d. As shown in the third panel of Fig. 3e, the temperature dependency of n_{Hall} changes abruptly near 60 K. In addition, the temperature-dependent mobility (μ) was also estimated with $V_{bg} = 0\text{ V}$ on the basis of the Drude model ($\sigma = \mu ne$) and is plotted in the fourth panel of Fig. 3e, where σ and n were obtained from the measured R_{xx} (Fig. 1d) and n_{Hall} (Fig. 3e), respectively. All the transport parameters in Fig. 3e exhibit critical changes near 60 K, which is in good agreement with the magnetic-phase transition of CGT at T_c . The consistency of the critical behavior of $\mu(T)$ with the magnetic phase transition also implies that it is affected by the magnetic-proximity effect and consequently becomes a relevant indicator for the phase transition.

We conducted a more in-depth analysis by examining the correlation among the transport parameters in Fig. 3e. Because the position of the R_{xx} peak for a given QH state is connected with the carrier density (n) and the magnetic field (H) from basic QH physics, we deliberately considered these two factors simultaneously by adopting the concept of a filling factor ν , defined as $\nu = nh/(e\mu_0 H)$. Figure 4a, b present the graph of R_{xx} and R_{xy} vs. the inverse of the filling factor (ν^{-1}) at different temperatures. The R_{xx} peak shift is clearly suppressed at low temperatures in Fig. 4a. Furthermore, the linearity of R_{xy} in weak magnetic fields is scaled

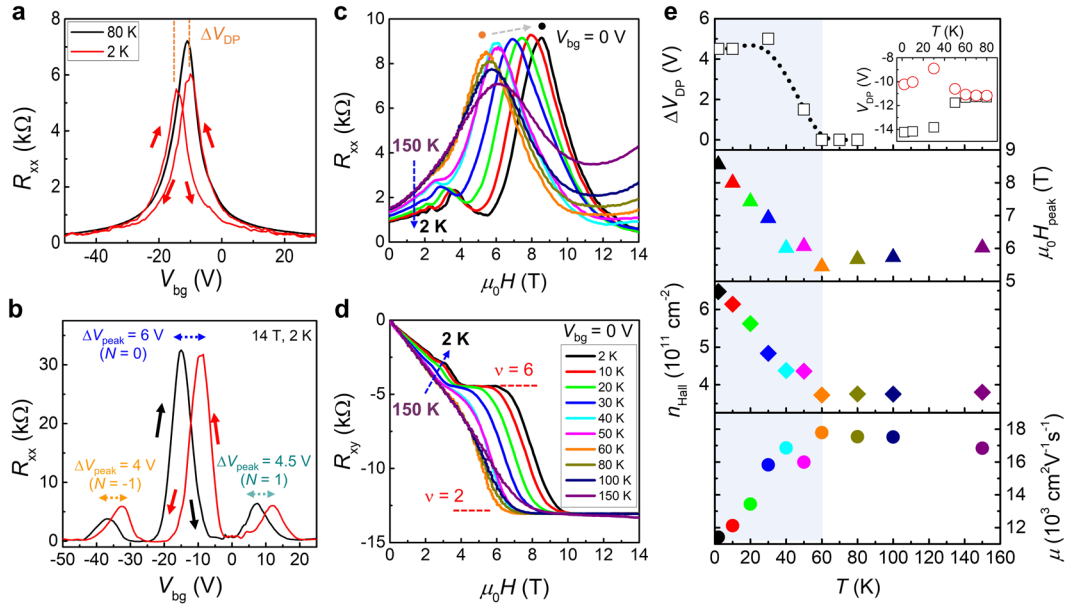


Fig. 3 Probing phase transition of CGT using temperature-dependent transport of D1. **a** R_{xx} vs. V_{bg} with 0 T at 80 K (black) and 2 K (red). **b** R_{xx} vs. V_{bg} with 2 K and 14 T, depending on sweeping direction. N indicates the Landau level index and ΔV_{peak} is the difference in the peak position for each N . **c**, **d** Temperature-dependent R_{xx} and R_{xy} vs. $\mu_0 H$ with $V_{bg} = 0$ V. **e** Temperature dependence of the extracted transport parameter ΔV_{DP} , which is obtained from the difference of V_{DP} for forward- (black squares) and backward- (red circles) gate sweeping in the inset. The black-dotted line is to guide the eye. $\mu_0 H_{peak}$ corresponds to the local maxima depicted by the dots in (c). Hall carrier density n_{Hall} is extracted by linear fitting from -1 T to 1 T of R_{xy} vs. $\mu_0 H$ in (d). Mobility μ is calculated using the Drude model, where R_{xx} in Fig. 1d and n_{Hall} in Fig. 3e are adopted.

with ν^{-1} irrespective of the temperature (Fig. 4b). These results indicate that the shifts of $\mu_0 H_{peak}$ and n_{Hall} in the second and the third panel of Fig. 3e have the same physical origin, which is the variation in the temperature-dependent carrier density under the influence of the ferromagnetic phase transition of CGT at its Curie temperature ($T_c \sim 61$ K)²⁵.

Furthermore, Fig. 4b reveals the evolution of additional QH states in relation with the phase transition of CGT. More specifically, R_{xy} is entirely linear at the high temperature of 150 K until it encounters the $\nu = 2$ QH plateau, but it deviates from that linearity as the temperature decreases. Finally, R_{xy} becomes quantized with the value of $h/6e^2$ corresponding to the $\nu = 6$ QH state. For the quantitative analysis, we differentiated R_{xy} with respect to ν^{-1} in Fig. 4c to verify the formation of the $\nu = 6$ QH plateau (i.e., $dR_{xy}/d\nu^{-1} \rightarrow 0$ as indicated in Fig. 4e for the conventional QH effect), and plotted the $dR_{xy}/d\nu^{-1}$ values for $\nu = 6$ as a function of temperature in Fig. 4d. Noticeably, $dR_{xy}/d\nu^{-1}$ is almost constant above T_c , but its magnitude starts to decrease as the temperature is lowered below T_c until it becomes $dR_{xy}/d\nu^{-1} \sim 0$ to form the clear $\nu = 6$ QH state at low temperatures.

This change can be interpreted concerning the magnetization in CGT coming into existence below T_c . A comparison of the evolution of the $\nu = 6$ QH state as a function of temperature in Fig. 4c with the other results in Figs. 1d and 3e show that all the transitions begin to occur near 60 K, which corresponds to the magnetic transition temperature of CGT. The total magnetic field, which, strictly speaking, is the magnetic flux density defined by $B = \mu_0(H+M)$ where M is the magnetization, is abruptly boosted by the ferromagnetic transition in CGT. This correspondence of the sudden change in n_{Hall} and the evolution of the $\nu = 6$ QH state is also observed in the other sample D2 (Supplementary Fig. 3). Other possibilities, such as parallel conduction through CGT, can be excluded by the typical temperature dependence of the QH effect as a function of ν . In addition, the result that the value of n_{Hall} increases with decreasing temperature precludes the contribution of thermal activation in CGT.

DISCUSSION

The essential observation in this work is that gate hysteresis is strongly correlated with the ferromagnetic phase transition of CGT. There are mainly two origins for gate hysteresis of graphene FET: charge trapping and capacitive gating⁴⁷. The two mechanisms give distinct hysteresis direction with V_{bg} , indicating that charge trapping is responsible for our case. Depending on charge trapping agents such as defect sites in graphene/substrate or adsorbate, the temperature dependence of gate hysteresis is distinguished^{48–51}. Because our pristine graphene in the device D1 has no significant temperature-dependent hysteresis, we can rule out the aforementioned origins. We also show in Supplementary Fig. 6 the back-gate voltage sweep data at room temperature of many other pristine graphene devices on SiO₂ and on h-BN/SiO₂ substrates. The non-hysteresis of the devices confirms that no extrinsic sources for the hysteresis are involved during the fabrication process in our experiment. As a result, the hysteresis can be utilized as a sensitive probe in this study. Furthermore, the critical occurrence of the gate hysteresis implies that ferromagnetic phase transition of CGT layer is indeed the origin for the gate hysteresis. Even though the microscopic mechanism for the spin-mediated trapping needs further theoretical work, signatures such as anomalous Hall effect (AHE) and exchange-induced state ($\nu = 4$) could exhibit its spin-related nature. Namely, even though the unclearly-defined CGT layers at the interface between graphene and CGT were formed as shown in Supplementary Fig. 1 of the TEM side-view image, we observed induced AHE feature and spin-polarized state for D1 as shown in Supplementary Figs. 7 and 8, respectively. Based on the discussion, we should emphasize that gate hysteresis becomes an appropriate parameter to detect phase transition of adjacent CGT layer, which can be expanded to other magnetic phases.

In addition to gate hysteresis, the other transport parameters can be employed to probe magnetic phase transition of ferromagnetic CGT; especially, T_c can be estimated by the electrical way. In fact, the seminal study for the magnetic proximity effect of graphene/CGT heterostructure has been

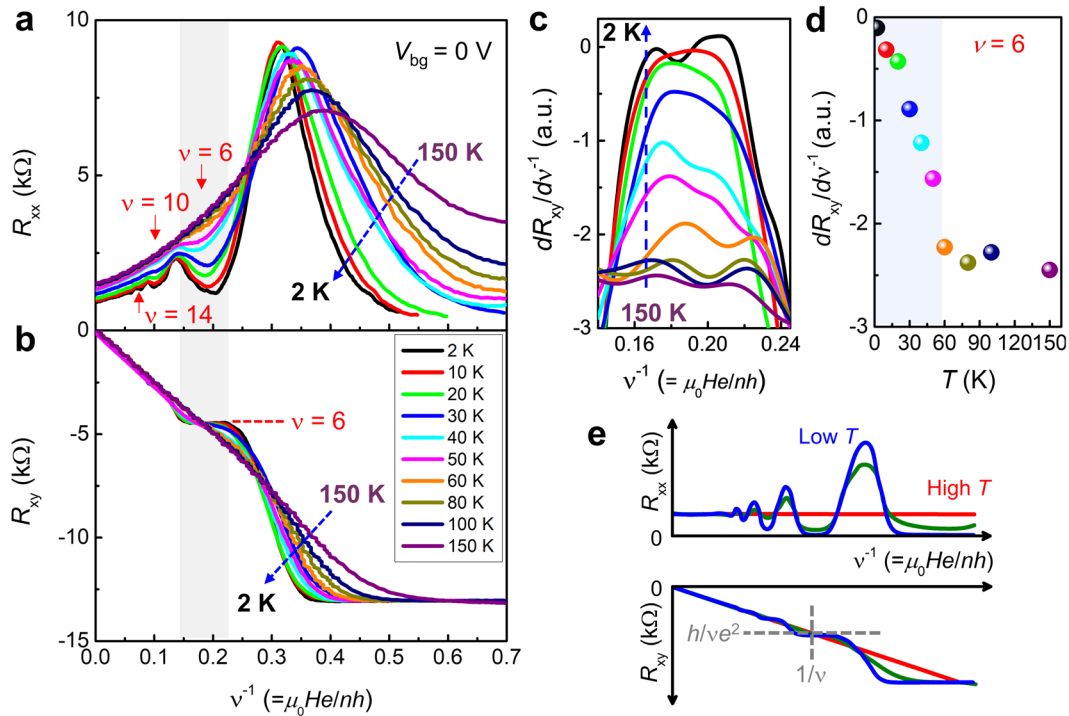


Fig. 4 Scaling of R_{xx} and R_{xy} in terms of ν^{-1} and magnetization-enhanced magnetic flux density (D1). **a, b** R_{xx} and R_{xy} vs. ν^{-1} ($=\mu_0 H_e / nh$) with respect to temperature. The gray shaded area indicates the region in which $\nu = 6$, where the typical temperature-dependent QH effect is observed. R_{xx} shows a fixed dip and R_{xy} crosses near $\nu = 6$, at a different temperature, in the gray region. Higher filling factors of 10 and 14 are indicated by red arrows. **c** Slope of R_{xy} vs. ν^{-1} (i.e. $dR_{xy}/d\nu^{-1}$) near $\nu = 6$ from 150 to 2 K. **d** Plot of temperature-dependent $dR_{xy}/d\nu^{-1}$ at $\nu = 6$. **e** Schematic of R_{xx} and R_{xy} vs. ν^{-1} for typical QHE of graphene with respect to temperature. At filling factor ν , R_{xy} evolves from linear (red) to plateau (blue) with decreasing temperature. At intermediate temperatures, R_{xy} deviates slightly from linearity near ν (green).

performed in terms of the Hanle spin precession experiment. Different from the nonlocal measurement configuration, we used local transport configuration and obtained a similar estimation for the magnetic phase transition of CGT. Consequently, a complementary understanding of the magnetic proximity in graphene/CGT heterostructure can be achieved with previous nonlocal transport³⁵.

In summary, we investigated the electrical transport properties of graphene under proximate coupling with a 2D ferromagnetic insulator, CGT, by forming a graphene/CGT heterostructure. Graphene is an appropriate contact electrode, making it feasible to measure the transport in pristine CGT. And the graphene/CGT heterostructure is suitable to detect the phase transition of CGT from its conductance variation. We found various pieces of evidence of successful proximity effects as discussed above. Furthermore, we observed the sudden emergence of an additional QH state, which can be attributed to additional magnetic flux density due to the magnetization of CGT. These results imply that graphene can sense the magnetic phase transition that occurs in adjacent CGT near T_c . Unlike many previous experiments regarding magnetic property measurements^{25,36,37}, the graphene transistor has the ability to detect electrical changes associated with magnetic phase-transition phenomena as a result of the proximity effect of the magnetic insulator. We foresee graphene-based vdW heterostructures to become an electrical platform for exploring various phases in magnetic insulators.

METHODS

Device fabrication

Graphene/CGT heterostructures were fabricated on a heavily *p*-doped silicon substrate, with a 300-nm-thick SiO_2 insulating layer, as follows. First,

h-BN flakes, with thicknesses in the range 20–40 nm, were exfoliated directly on the SiO_2/Si substrate. Monolayer graphene was obtained via mechanical exfoliation on the PMMA/PVA/ SiO_2/Si substrate, where poly (methyl methacrylate) (PMMA) and poly(vinyl alcohol) (PVA) is coated and then transferred onto the h-BN/ SiO_2/Si substrate. Subsequently, the graphene was etched by oxygen plasma (3 mTorr and 30 W) for D1 and D2 to construct the Hall-bar structure and the graphene electrode. Metal-electrode patterning was performed using electron-beam lithography, followed by Cr/Au (5/50 nm) evaporation under high-vacuum conditions ($\sim 10^{-6}$ Torr). The graphene device on h-BN was annealed in forming gas (H_2 , Ar) at 300 °C for 4 h to remove contamination on the graphene surface. Second, CGT, with a thickness of a few tens of nanometers, was transferred onto the graphene devices. CGT flake was exfoliated from the single crystal (HQ graphene, Netherland) and immediately transferred to avoid oxidation at the interface. Finally, a thick h-BN layer was placed on top of the device soon after transferring the CGT, to prevent oxidation of the latter.

Device characterization

We recorded the Raman spectra with a 532-nm laser under ambient conditions (Renishaw Inc., UK). The TEM cross-sectional experiment was carried out using a high-resolution TEM (JEM ARM 200 F, JEOL, Japan). The DC electrical characteristics of the pristine CGT (and graphene), and graphene/CGT were analyzed under high vacuum ($\sim 10^{-6}$ Torr) in a cryostat (Physical Property Measurement System (PPMS), Quantum Design Inc., USA) with a semiconductor parameter analyzer (4200SCS, Keithley Instruments Inc., USA). We gently annealed the devices at 400 K for approximately 2 h in high vacuum (approximately 10^{-6} Torr) before the electrical measurements.

DATA AVAILABILITY

The data that support the findings of this study are available from the corresponding author upon reasonable request.

Received: 17 November 2021; Accepted: 10 February 2022;
Published online: 14 March 2022

REFERENCES

- Dean, C. R. et al. Boron nitride substrates for high-quality graphene electronics. *Nat. Nanotechnol.* **5**, 722–726 (2010).
- Du, X. et al. Fractional quantum Hall effect and insulating phase of Dirac electrons in graphene. *Nature* **462**, 192–195 (2009).
- Bolotin, K. I. et al. Observation of the fractional quantum Hall effect in graphene. *Nature* **462**, 196–199 (2009).
- Cao, Y. et al. Unconventional superconductivity in magic-angle graphene superlattices. *Nature* **556**, 43–50 (2018).
- Cao, Y. et al. Correlated insulator behaviour at half-filling in magic-angle graphene superlattices. *Nature* **556**, 80–84 (2018).
- Yankowitz, M. et al. Emergence of superlattice Dirac points in graphene on hexagonal boron nitride. *Nat. Phys.* **8**, 382–386 (2012).
- Ponomarenko, L. A. et al. Cloning of Dirac fermions in graphene superlattices. *Nature* **497**, 594–594 (2013).
- Dean, C. R. et al. Hofstadter's butterfly and the fractal quantum Hall effect in moiré superlattices. *Nature* **497**, 598–602 (2013).
- Schmidt, H., Rode, J. C., Smirnov, D. & Haug, R. J. Superlattice structures in twisted bilayers of folded graphene. *Nat. Commun.* **5**, 5742 (2014).
- Cao, Y. et al. Superlattice-induced insulating states and valley-protected orbits in twisted bilayer graphene. *Phys. Rev. Lett.* **117**, 116804 (2016).
- Kim, Y. et al. Charge inversion and topological phase transition at a twist angle induced van Hove singularity of bilayer graphene. *Nano Lett.* **16**, 5053–5059 (2016).
- Park, N. et al. Ferroelectric single-crystal gated graphene/hexagonal-BN/ferroelectric field-effect transistor. *ACS Nano* **9**, 10729–10736 (2015).
- Wei, P. et al. Strong interfacial exchange field in the graphene/EuS heterostructure. *Nat. Mater.* **15**, 711–716 (2016).
- Sakai, S. et al. Proximity-induced spin polarization of graphene in contact with half-metallic manganite. *ACS Nano* **10**, 7532–7541 (2016).
- Tang, C. et al. Approaching quantum anomalous Hall effect in proximity-coupled YIG/graphene/h-BN sandwich structure. *APL Mater.* **6**, 026401 (2017).
- Song, H.-D. et al. Electrical control of magnetic proximity effect in a graphene/multiferroic heterostructure. *Appl. Phys. Lett.* **113**, 183101 (2018).
- Song, H.-D. et al. Asymmetric modulation on exchange field in a graphene/BiFeO₃ heterostructure by external magnetic field. *Nano Lett.* **18**, 2435–2441 (2018).
- Wu, Y.-F. et al. Magnetic proximity effect in graphene coupled to a BiFeO₃ nanoplate. *Phys. Rev. B* **95**, 195426 (2017).
- Wang, Z. et al. Proximity-induced ferromagnetism in graphene revealed by the anomalous Hall effect. *Phys. Rev. Lett.* **114**, 016603 (2015).
- Song, G., Ranjbar, M., Daughton, D. R. & Kiehl, R. A. Nanoparticle-induced anomalous Hall effect in graphene. *Nano Lett.* **19**, 7112–7118 (2019).
- Averyanov, D. V. et al. High-temperature magnetism in graphene induced by proximity to EuO. *ACS Appl. Mater. Interfaces* **10**, 20767–20774 (2018).
- Cheng, G. et al. Graphene in proximity to magnetic insulating LaMnO₃. *Appl. Phys. Lett.* **105**, 133111 (2014).
- Wu, Y. et al. Large exchange splitting in monolayer graphene magnetized by an antiferromagnet. *Nat. Electron.* **3**, 604–611 (2020).
- Mermin, N. D. & Wagner, H. Absence of ferromagnetism or antiferromagnetism in one- or two-dimensional isotropic Heisenberg models. *Phys. Rev. Lett.* **17**, 1133–1136 (1966).
- Gong, C. et al. Discovery of intrinsic ferromagnetism in two-dimensional van der Waals crystals. *Nature* **546**, 265–269 (2017).
- Huang, B. et al. Layer-dependent ferromagnetism in a van der Waals crystal down to the monolayer limit. *Nature* **546**, 270–273 (2017).
- Deng, Y. et al. Gate-tunable room-temperature ferromagnetism in two-dimensional Fe₃GeTe₂. *Nature* **563**, 94–99 (2018).
- Burch, K. S., Mandrus, D. & Park, J.-G. Magnetism in two-dimensional van der Waals materials. *Nature* **563**, 47–52 (2018).
- Gong, C. & Zhang, X. Two-dimensional magnetic crystals and emergent heterostructure devices. *Science* **363**, eaav4450 (2019).
- Gibertini, M., Koperski, M., Morpurgo, A. F. & Novoselov, K. S. Magnetic 2D materials and heterostructures. *Nat. Nanotechnol.* **14**, 408–419 (2019).
- Haugen, H., Huertas-Hernando, D. & Brataas, A. Spin transport in proximity-induced ferromagnetic graphene. *Phys. Rev. B* **77**, 115406 (2008).
- Singh, S. et al. Strong modulation of spin currents in bilayer graphene by static and fluctuating proximity exchange fields. *Phys. Rev. Lett.* **118**, 187201 (2017).
- Leutenantsmeyer, J. C., Kaverzin, A. A., Wojtaszek, M. & van Wees, B. J. Proximity induced room temperature ferromagnetism in graphene probed with spin currents. *2D Mater.* **4**, 014001 (2016).
- Zollner, K., Gmitra, M. & Fabian, J. Electrically tunable exchange splitting in bilayer graphene on monolayer Cr₂X₂Te₆ with X = Ge, Si, and Sn. *N. J. Phys.* **20**, 073007 (2018).
- Karpiak, B. et al. Magnetic proximity in a van der Waals heterostructure of magnetic insulator and graphene. *2D Mater.* **7**, 015026 (2019).
- Xing, W. et al. Electric field effect in multilayer Cr₂Ge₂Te₆: a ferromagnetic 2D material. *2D Mater.* **4**, 024009 (2017).
- Wang, Z. et al. Electric-field control of magnetism in a few-layered van der Waals ferromagnetic semiconductor. *Nat. Nanotechnol.* **13**, 554–559 (2018).
- Escolar, J. et al. Anisotropic magnetoconductance and Coulomb blockade in defect engineered Cr₂Ge₂Te₆ van der Waals heterostructures. *Phys. Rev. B* **100**, 054420 (2019).
- Ji, H. et al. A ferromagnetic insulating substrate for the epitaxial growth of topological insulators. *J. Appl. Phys.* **114**, 114907 (2013).
- Hao, Z. et al. Atomic scale electronic structure of the ferromagnetic semiconductor Cr₂Ge₂Te₆. *Sci. Bull.* **63**, 825–830 (2018).
- Heo, J. et al. Nonmonotonic temperature dependent transport in graphene grown by chemical vapor deposition. *Phys. Rev. B* **84**, 035421 (2011).
- Özyilmaz, B. et al. Electronic transport and quantum Hall effect in bipolar graphene p-n-p junctions. *Phys. Rev. Lett.* **99**, 166804 (2007).
- Yamada, T. et al. Field emission characteristics from graphene on hexagonal boron nitride. *Appl. Phys. Lett.* **104**, 221603 (2014).
- Kaushik, N. et al. Reversible hysteresis inversion in MoS₂ field effect transistors. *npj 2D Mater. Appl.* **1**, 34 (2017).
- Zhang, Y., Tan, Y.-W., Stormer, H. L. & Kim, P. Experimental observation of the quantum Hall effect and Berry's phase in graphene. *Nature* **438**, 201–204 (2005).
- Giesbers, A. J. M. et al. Quantum-Hall activation gaps in graphene. *Phys. Rev. Lett.* **99**, 206803 (2007).
- Wang, H. et al. Hysteresis of electronic transport in graphene transistors. *ACS Nano* **4**, 7221–7228 (2010).
- Yoo, J. S., Park, Y. W., Skákalová, V. & Roth, S. Shubnikov-de Haas and Aharonov Bohm effects in a graphene nanoring structure. *Appl. Phys. Lett.* **96**, 143112 (2010).
- Barthold, P., Lüdtke, T., Schmidt, H. & Haug, R. J. Low-temperature hysteresis in the field effect of bilayer graphene. *N. J. Phys.* **13**, 043020 (2011).
- Kang, H. et al. Quantum Hall conductance of graphene combined with charge-trap memory operation. *Nanotechnology* **26**, 345202 (2015).
- Mohrmann, J., Watanabe, K., Taniguchi, T. & Danneau, R. Persistent hysteresis in graphene-mica van der Waals heterostructures. *Nanotechnology* **26**, 015202 (2014).

ACKNOWLEDGEMENTS

This work was supported by the Technology Innovation Program (No. 20006492 (D.S.)) funded by the Ministry of Trade, Industry & Energy and by the National Research Foundation (NRF-2019R11A1A01058123 (S.J.H.), NRF-2021R1A4A5031762 (S.J.H.), NRF-2021R1A2C2013289 (H.K.) and NRF-2021R1A2C2005281 (D.S.)) funded by the Ministry of Science and ICT, Republic of Korea.

AUTHOR CONTRIBUTIONS

T.K.C., S.J.H., and D.S. conceived the experiment. T.K.C. fabricated the devices and S.J.H., T.K.C. and D.S. performed the measurements and analysed the data with H.K. The manuscript was written by all participating authors.

COMPETING INTERESTS

The authors declare no competing interests.

ADDITIONAL INFORMATION

Supplementary information The online version contains supplementary material available at <https://doi.org/10.1038/s41535-022-00435-9>.

Correspondence and requests for materials should be addressed to Dongseok Suh.

Reprints and permission information is available at <http://www.nature.com/reprints>

Publisher's note Springer Nature remains neutral with regard to jurisdictional claims in published maps and institutional affiliations.



Open Access This article is licensed under a Creative Commons Attribution 4.0 International License, which permits use, sharing, adaptation, distribution and reproduction in any medium or format, as long as you give appropriate credit to the original author(s) and the source, provide a link to the Creative Commons license, and indicate if changes were made. The images or other third party material in this article are included in the article's Creative Commons license, unless indicated otherwise in a credit line to the material. If material is not included in the article's Creative Commons license and your intended use is not permitted by statutory regulation or exceeds the permitted use, you will need to obtain permission directly from the copyright holder. To view a copy of this license, visit <http://creativecommons.org/licenses/by/4.0/>.

© The Author(s) 2022